MNRAS **445,** 115–127 (2014) doi:10.1093/mnras/stu1616

Systematic variations of central mass density slopes in early-type galaxies

C. Tortora,[1⋆] F. La Barbera,[1] N. R. Napolitano,[1] A. J. Romanowsky,[2,3] I. Ferreras[4] and R. R. de Carvalho[5]

[1] *INAF – Osservatorio Astronomico di Capodimonte, Salita Moiariello, 16, I-80131 Napoli, Italy*
[2] *Department of Physics and Astronomy, San José State University, San Jose, CA 95192, USA*
[3] *University of California Observatories, 1156 High Street, Santa Cruz, CA 95064, USA*
[4] *Mullard Space Science Laboratory, University College London, Holmbury St Mary, Dorking, Surrey RH5 6NT, UK*
[5] *Instituto Nacional de Pesquisas Espaciais/MCTI Av. dos Astronautas 1758, Jd. Granja São José dos Campos - 12227-010 SP, Brazil*

Accepted 2014 August 7. Received 2014 July 17; in original form 2014 May 17

ABSTRACT

We study the total density distribution in the central regions ($\lesssim$1 effective radius, R_e) of early-type galaxies (ETGs), using data from SPIDER and ATLAS^{3D}. Our analysis extends the range of galaxy stellar mass ($M_\star$) probed by gravitational lensing, down to $\sim 10^{10}\,M_\odot$. We model each galaxy with two components (dark matter halo + stars), exploring different assumptions for the dark matter halo profile (i.e. NFW, NFW-contracted, and Burkert profiles), and leaving stellar mass-to-light ($M_\star/L$) ratios as free fitting parameters to the data. For all plausible halo models, the best-fitting $M_\star/L$, normalized to that for a Chabrier initial mass function, increases systematically with galaxy size and mass. For an NFW profile, the slope of the total mass profile is non-universal, independently of several ingredients in the modelling (e.g. halo contraction, anisotropy, and rotation velocity in ETGs). For the most massive ($M_\star \sim 10^{11.5}\,M_\odot$) or largest ($R_e \sim 15$ kpc) ETGs, the profile is isothermal in the central regions ($\sim R_e/2$), while for the low-mass ($M_\star \sim 10^{10.2}\,M_\odot$) or smallest ($R_e \sim 0.5$ kpc) systems, the profile is steeper than isothermal, with slopes similar to those for a constant-M/L profile. For a steeper concentration–mass relation than that expected from simulations, the correlation of density slope with galaxy mass tends to flatten, while correlations with R_e and velocity dispersions are more robust. Our results clearly point to a 'non-homology' in the total mass distribution of ETGs, which simulations of galaxy formation suggest may be related to a varying role of dissipation with galaxy mass.

Key words: galaxies: elliptical and lenticular, cD – galaxies: evolution – galaxies: general.

1 INTRODUCTION

In the so-called Λ cold dark matter (ΛCDM) model, the formation of virialized dark matter (DM) haloes proceeds from the initial expansion and subsequent collapse of tiny density perturbations. The assembly and evolution of DM haloes can be studied in detail by means of *N*-body simulations, which predict that the DM density profile, $\rho_{DM}(r)$, should be independent of halo mass, being well described by a double power-law relation – the so-called NFW profile – with $\rho_{DM}(r) \propto r^{-3}$ in the outer regions, and $\rho_{DM}(r) \propto r^{\alpha}$, with $\alpha < 0$, in the centre ($\alpha = -1$, Navarro, Frenk & White 1996; $\alpha = -1.5$, Moore et al. 1998). However, *N*-body simulations follow only the evolution of DM particles, not including the extremely complex physics of gas and stars. These components are dominant in the central regions of galaxies, in particular those of early-type galaxies (ETGs), which exhibit a peaked surface brightness profile, typically well described by the Sérsic law (Ciotti 1991), with a shape parameter, n (Sérsic index), that accounts for variations of the light profile shape among galaxies. Gas and stars, falling down into the DM potential well, could drag a significant amount of DM particles inside, making the DM profile more concentrated in the galaxy centre (Blumenthal et al. 1986; Gnedin et al. 2004; Del Popolo 2009; Cardone et al. 2011b) than the 'expected' NFW law. The study of the DM profile in the inner regions of ETGs is also hampered by the degeneracy between the shape of the DM profile and that of the stellar initial mass function (IMF; Napolitano, Romanowsky & Tortora 2010; Dutton et al. 2011; Dutton, Mendel & Simard 2012; Tortora, Romanowsky & Napolitano 2013).

For massive galaxies ($M_\star \sim 10^{11-12}\,M_\odot$), gravitational lensing and studies of stellar dynamics in the galaxy central regions have found that the light and halo profiles conspire to have a total-mass density profile which is nearly isothermal (Bolton et al. 2006, 2008;

⋆ E-mail: ctortora@na.astro.it

Auger et al. 2009, 2010; Chae, Bernardi & Kravtsov 2014; Oguri, Rusu & Falco 2014), i.e. a total-mass density slope of $\alpha \sim -2$. The crucial questions here are why there is such a conspiracy, and if it is universal (i.e. holds for all galactic systems). Indeed, observations suggest that this is not the case. For low-mass ETGs, Dutton & Treu (2014) have recently shown that density profiles are steeper than isothermal, while they are isothermal for high-mass systems. At the mass scale of groups and clusters of galaxies, the mass density distributions appear to be also shallower than isothermal (e.g. Sand et al. 2008; Humphrey & Buote 2010). de Blok et al. (2001) also found shallower-than-isothermal profiles in low-surface-brightness galaxies (with $\alpha \sim 0$). The recent theoretical work by Remus et al. (2013) seems to provide a theoretical framework to interpret these results. Their simulations show that *in situ* star formation, resulting from dissipative processes, tends to form steeper-than-isothermal profiles, while gas-poor mergers are a natural attractor towards the isothermal slope. This motivates for further, in-depth, studies of the slope of total-mass density profiles and their correlations with galaxy properties, while making connections to the theory.

In this work, we study the slope of the mass density profile of ETGs in a wide mass range, using data from the SDSS-based SPIDER survey (La Barbera et al. 2010), one of the largest well-characterized samples of ETGs in the nearby Universe – with high-quality spectroscopy and optical plus near-infrared (NIR) photometry available – as well as the ATLAS^{3D} sample (Cappellari et al. 2011). We probe the galaxy mass profiles down to a stellar mass of $10^{10}\,M_{\odot}$, hence extending, with an independent approach, results of gravitational lensing studies for massive galaxies (Bolton et al. 2006, 2008; Auger et al. 2009, 2010). We perform a Jeans dynamical analysis of the available photometric and spectroscopic data, with a suite of dynamical models (see Tortora et al. 2013), testing several assumptions on the shape of the DM halo profile and leaving stellar mass-to-light ratios as free parameters in the analysis. Our work complements previous studies (e.g. Humphrey & Buote 2010; Dutton & Treu 2014), in that it compares findings for two independent, well-characterized, samples of ETGs, and investigates the impact of a variety of modelling ingredients. Our goal is to scrutinize if the central density slope of the total mass distribution in ETGs stays isothermal or changes with mass and other galaxy properties, comparing to predictions of simulations of galaxy formation.

The paper is organized as follows. In Section 2, we present the samples of ETGs used in this study. Section 3 deals with data analysis, describing the dynamical modelling approach and our definitions of the mass density slope. Sections 4 and 5 present the correlations of the mass-to-light ratio and total-mass density slope with galaxy properties, i.e. structural parameters, velocity dispersion, stellar mass, and DM fraction. In Section 6, we present an extensive comparison of our results with those from the literature. Section 7 summarizes results and conclusions.

2 SAMPLES

We rely on two samples of ETGs, one main sample from the SPIDER survey (La Barbera et al. 2010), and a complementary data set from the ATLAS^{3D} project (Cappellari et al. 2011).

2.1 SPIDER sample

The SPIDER data set is described in La Barbera et al. (2010). It consists of a sample of 5080 bright ($M_r < -20$) ETGs, in the redshift range of $z = 0.05$–0.095, with optical and NIR photometry available (*grizYJHK* wavebands) from the Sloan Digital Sky Survey (SDSS) DR6 and the UKIRT Infrared Deep Sky Survey-Large Area Survey DR3.[1] Structural parameters, i.e. the effective radius R_e and Sérsic index n, have been measured homogeneously for all galaxies, from g through K, using the software 2DPHOT (La Barbera et al. 2008). SPIDER ETGs have central velocity dispersions, σ_{Ap}, available from the SDSS, measured in the circular aperture of the SDSS fibre (having radius $R_{Ap} = 1.5$ arcsec). The median ratio of the SDSS fibre to the K-band effective radius, R_{Ap}/R_e, amounts to $\sim$0.6, implying only a mild extrapolation in the estimate of mass density slopes (see below).

ETGs are defined as bulge-dominated systems (i.e. SDSS parameter $\mathrm{fracDev}_r > 0.8$, where $\mathrm{fracDev}_r$ measures the fraction of galaxy light better fitted by a de Vaucouleurs, rather than an exponential law), featuring passive spectra within the SDSS fibres (SDSS attribute $\mathrm{eClass} < 0$, where eClass indicates the spectral type of a galaxy based on a principal component analysis). For this work, we rely on a subsample of $\sim$4300 SPIDER ETGs, with better quality optical and NIR structural parameters, selected as in Tortora et al. (2012). For each galaxy, the stellar mass-to-light ratio, $\Upsilon_\star$, has been estimated by fitting Bruzual & Charlot (2003) stellar population models to the multiband photometry, under the assumption of a Chabrier IMF (see Swindle et al. 2011 and Tortora et al. 2012 for details). The sample is 95 per cent complete down to a stellar mass of $M_\star \sim 3 \times 10^{10}\,M_{\odot}$.

2.2 ATLAS^{3D} sample

Our second sample consists of 260 ETGs from the ATLAS^{3D} survey (Cappellari et al. 2013a,b). Further details about the selection of ATLAS^{3D} galaxies are provided in Tortora et al. (2014). For each galaxy, we perform the dynamical analysis by using (i) its r-band effective radius, R_e, (ii) the r-band total luminosity L_r, (iii) the projected stellar velocity dispersion, σ_e, within R_e, and (iv) the stellar mass-to-light ratio (Υ_*) derived by fitting galaxy spectra with Vazdekis et al. (2012) single SSP MILES models, having a Salpeter (1955) IMF. Stellar masses are converted to a Chabrier (2001) IMF, using the fact that the Chabrier IMF normalization is $\sim$0.26 dex smaller than the Salpeter one. We notice that out of 260 ETGs, about 15 per cent of ATLAS^{3D} ETGs have significant stellar mass-to-light ratio gradients and young stellar populations (with an Hβ equivalent width $>$2.3 Å). We found that excluding these objects from the analysis does not affect at all the trends of total-mass density slope.

As discussed in Tortora et al. (2014), it is important to note that the published L_r and R_e values are not self-consistent. The former correspond to detailed multi-Gaussian expansion (MGE) fits that were truncated at typically $\sim 4\,R_e$. The latter are the MGE-based values renormalized by a factor of 1.35 to correspond to more conventional estimates from the literature. Here, we will use these R_e values, but adjust each L_r value such that the projected luminosity inside R_e for our adopted de Vaucouleurs (1948) model is the same as in the original MGE model. This means increasing L_r by typically a factor of 1.2.

[1] http://www.sdss.org, http://www.ukidss.org

3 ANALYSIS

3.1 Dynamical modelling

We derive the dynamical (i.e. total) mass distribution of ETGs by solving spherical isotropic Jeans equations, where a given model for the mass profile is fitted to $\sigma_{\rm Ap}$ and $\sigma_{\rm e}$, for SPIDER and ATLAS$^{\rm 3D}$ ETGs, respectively. We use two-component mass models, describing stars and DM.

The stellar mass profile is modelled by either a Sérsic (SPIDER) or a de Vaucouleurs (ATLAS$^{\rm 3D}$) law. The shape parameter n and effective radius of the Sérsic laws are those obtained by fitting galaxy images in K band (see Section 2). For the de Vaucouleurs law, we use r-band effective radii from the ATLAS$^{\rm 3D}$ sample. In both cases, the total luminosity of the light distribution is converted into stellar mass by means of the stellar mass-to-light ratio, Υ_*, which is a free fitting parameter.[2] This procedure assumes that the shape and scale radius of the stellar mass distribution of ETGs are the same as for the light distribution, i.e. one can neglect Υ_* gradients inside these galaxies. One can notice that although Sérsic fits are known to provide a better fit to the light distribution of ETGs than a pure de Vaucouleurs law, a comparison of results for Sérsic (SPIDER) versus de Vaucouleurs (ATLAS$^{\rm 3D}$) profiles is useful to test the robustness of the results against the parametrization of the galaxy light distribution. Also, K-band light is more sensitive to the old quiescent component of an unresolved stellar population, describing more closely the stellar mass profile of a galaxy, than the light distribution at optical wavebands. Hence, the comparison of K- (SPIDER) and r- (ATLAS$^{\rm 3D}$) band results allows us to test the impact of stellar mass-to-light ratio gradients in galaxies, besides that of selecting two different samples of ETGs, and using different parametrizations of the galaxy light profiles. As a further test, we also compare our findings to those obtained for the (same) SPIDER sample using (SDSS-based) de Vaucouleurs (rather than Sérsic) structural parameters in the r (rather than K) band. In general, as discussed below, assuming a constant Υ_* does not likely affect significantly our conclusions.

For the DM component, in the case of the SDSS-based SPIDER sample, we can rely only on velocity dispersions measured within a single aperture (i.e. the SDSS fibre), which does not allow us to constrain the shape of the DM profile in detail. In contrast, using the spatially extended kinematics of ATLAS$^{\rm 3D}$ galaxies, one could constrain, in principle, the shape of both the stellar and DM components in the central galaxy regions in detail, as shown, e.g. in Cappellari et al. (2012). In this work, to perform a clean comparison of results from both samples, we apply the same procedure to both SPIDER and ATLAS$^{\rm 3D}$ ETGs, fitting two-component models to central velocity dispersion estimates for both samples. To this effect, we explore a variety of models for the DM component, exploring several plausible assumptions (Tortora et al. 2013).

Navarro et al. (1996, *hereafter NFW) profiles*. The DM profile from N-body simulations is well described by a double power law, commonly referred to as the NFW profile (NFW; Navarro, Frenk & White 1997). In this work, we adopt the NFW as the reference DM profile, assuming also the correlation between virial mass and concentration ($M_{\rm vir}$ and $c_{\rm vir}$, respectively), that applies to a *WMAP*5 cosmology (Macciò, Dutton & van den Bosch 2008) as well as the $M_{\rm vir}$–$M_\star^{\rm Chab}$ correlation from Moster et al. (2010). In order to explore the effect of a possible modification to the DM profile because of the interaction between gas and stars with DM, we also consider the case of an NFW with an adjustable degree of baryon-induced adiabatic contraction (AC, Gnedin et al. 2004). Also, we explore how our results depend on the assumed $M_{\rm vir}$–$c_{\rm vir}$ relation, by (i) adopting a constant $M_{\rm vir}= 10^{13}\,{\rm M}_\odot$ (and deriving the corresponding, constant, $c_{\rm vir}$ from the Macciò et al. 2008 $M_{\rm vir}$–$c_{\rm vir}$ relation), and (ii) using the $c_{\rm vir}$–$M_{\rm vir}$ correlation, based on observations, from Leier, Ferreras & Saha (2012, hereafter LFS12). In the latter case, we adopt the relation obtained from LFS12 by combining X-ray results from Buote et al. (2007) with a gravitational lensing analysis of galaxies at intermediate redshifts.[3] For the median redshift of the SPIDER sample ($z\sim 0.08$), the relation is written as $c_{\rm vir} = 9.62 \times {M_{\rm vir}}^{-0.278}$. Note that although LFS12 found some evidence for a variation of the slope of the $M_{\rm vir}$–$c_{\rm vir}$ relation with the $M_{\rm vir}$ range fitted, this is unimportant for the relatively narrow mass range covered by our sample of ETGs with respect to that of LFS12. As discussed below, the LFS12 relation is significantly steeper than the Macciò et al. (2008) one, providing significantly higher concentrations for the lowest mass galaxies analysed in this work. Also, LFS12 assumed a Milky Way (MW)-like, Chabrier, IMF to map the stellar mass distribution of lensing galaxies, while in this study, we keep the Υ_* (i.e. the 'IMF normalization') as a free fitting parameter. In the following, we refer to models with NFW profiles and a $c_{\rm vir}$–$M_{\rm vir}$ relation from LFS12 as 'high-concentration' NFW models.

Burkert (1995) profiles. The Burkert profile is the prototype of cored models, and has been shown to reproduce quite well the DM profile of spirals and dwarf galaxies. The density and scale parameter of the Burkert profile ($\rho_{\rm B}$ and $r_{\rm B}$, respectively) are assumed to follow the $\rho_{\rm B}-r_{\rm B}$ relation from Salucci & Burkert (2000), adjusted to match results at higher surface density, for two ETGs, by Memola, Salucci & Babić (2011, hereafter MSB11). We explore two cases in detail, where the scale radius is set to $r_{\rm B} = 1$ and 20 kpc, respectively. The possible impact of a varying $r_{\rm B}$ (with, e.g. galaxy mass) on our results is discussed in Section 5.2.

For each galaxy and a given DM model, one has one single fitting parameter, i.e. the mass-to-light ratio Υ_*. The Υ_* is constrained by solving the Jeans equations to match the available velocity dispersion estimate (see above). We have performed several tests, showing that our results are quite independent of the assumptions on the DM profile. None of the conclusions is changed when comparing results for NFW profiles with either a constant $M_{\rm vir}= 10^{13}\,{\rm M}_\odot$ (and constant $c_{\rm vir}$), or the Macciò et al. (2008) $c_{\rm vir}$–$M_{\rm vir}$ relation. However, assuming a cored Burkert profile or high-concentration haloes – consistent with LFS12 – can affect significantly some of our results, as discussed below.

3.2 Inferring the slope of the density profile

We aim here to study the slope of the total mass profile of ETGs, rather than that of DM only (as in our previous work, see Napolitano et al. 2010). For each galaxy, at a given (deprojected) galactocentric distance, r, the total-mass density, $\rho(r)$, is obtained by summing the best-fitting stellar mass profile and the DM profile at that radius.

[2] Note that stellar mass-to-light ratios estimated from stellar population models (Section 2) are not used to derive the density slopes, but only as reference values to normalize the best-fitting Υ_*s, and to produce correlations of density slope with stellar-mass estimates for a 'standard' (i.e. MW-like) IMF (allowing a more direct comparison to other studies).

[3] We used the equation 11 from LFS12, with the *comb* best-fitting slope and normalization coefficients from their table 1.

In order to probe the robustness of the correlations between mass-density slope and galaxy properties, we adopt different definitions of the slope.

(i) We define the local logarithmic slope of the profile, $\alpha_{\rm l}(r) = {\rm d}\log\rho(r)/{\rm d}\log r$.

(ii) We compute the *mass-weighted logarithmic slope*, $\alpha_{\rm mw}$, within a given radius r (Koopmans et al. 2009; Dutton & Treu 2014). It is defined as

$$\alpha_{\rm mw}(r) \equiv \frac{1}{M(r)}\int_0^r \alpha_{\rm l}(r) 4\pi x^2 \rho(x){\rm d}x = -3 + \frac{4\pi r^3\rho(r)}{M(r)}, \quad (1)$$

where $M(r)$ is the (total) mass enclosed within a sphere of radius r. Some algebra shows that

$$\alpha_{\rm mw}(r) = -3 + {\rm d}\log M(r)/{\rm d}\log r. \quad (2)$$

For a power-law density profile, $\rho \propto r^{\alpha}$, one has $\alpha_{\rm l}(r) = \alpha_{\rm mw}(r) = \alpha$ at all radii, while this is not true for a general density distribution. However, in general, one can demonstrate that $\alpha_{\rm mw}(r) > \alpha$. We calculate the logarithmic slope at two different radii, i.e. $R_{\rm e}/2$ and $R_{\rm e}$, respectively, while the mass-weighted slope is computed within $r = R_{\rm e}$. These choices are motivated by the fact that the available estimates of velocity dispersion refer to an aperture with radius ranging from a few tenths of $R_{\rm e}$ to about one $R_{\rm e}$, for both the SPIDER and ATLAS$^{\rm 3D}$ samples. Thus, our choice minimizes the amount of extrapolation of the best-fitting mass models, exploring at the same time the inner profile at different radii ($R_{\rm e}/2$ and $R_{\rm e}$).

In the following sections, we will discuss these slopes in terms of $R_{\rm e}$, Sérsic n, $\sigma_{\rm e}$, stellar mass, and central DM fraction within a radius R, defined as $f_{\rm DM}(R) = 1 - M_{\star}(R)/M_{\rm tot}(R)$.

4 MASS-TO-LIGHT RATIO TRENDS

Using the dynamical estimate of Υ_* (see Section 3), we define the mismatch parameter, $\delta_{\rm IMF} = \Upsilon_{\star}/\Upsilon_{\star}^{\rm Chab}$, where $\Upsilon_*^{\rm Chab}$ is the stellar mass-to-light ratio obtained by fitting data (either colours or galaxy spectra) with stellar population models having a Chabrier IMF. The $\delta_{\rm IMF}$ can be interpreted as a variation in the normalization of the IMF with respect to the case of a 'standard', MW-like, distribution.

Fig. 1 plots the mismatch parameter as a function of $R_{\rm e}$, Sérsic index n, $\sigma_{\rm e}$, and $M_{\star}$, the latter estimated with either $\Upsilon_*^{\rm Chab}$ (i.e. a Chabrier IMF, $M_{\star}^{\rm Chab}$) or Υ_* (i.e. the best-fitting IMF normalization, $M_{\star}$). We find that $\delta_{\rm IMF}$ is positively correlated with $R_{\rm e}$, $\sigma_{\rm e}$, and $M_{\star}$, becoming larger than 1 in more massive and bigger galaxies. In contrast, the $\delta_{\rm IMF}$ decreases with n, while it is almost constant with $M_{\star}^{\rm Chab}$. The trends for Burkert and 'high-concentration' NFW models encompass the range of values for all trends. Although the absolute value of $\delta_{\rm IMF}$ depends on the adopted DM profile in the modelling, the relative trends of $\delta_{\rm IMF}$ trends with galaxy parameters are robust, being independent of the assumptions on the DM model (e.g. NFW versus AC+NFW versus Burkert profiles), and the assumed $c_{\rm vir}$–$M_{\rm vir}$ relation.

The mismatch parameter for ATLAS$^{\rm 3D}$ using the fiducial NFW+Sérsic galaxy model is also shown. All the correlations are shallower, and Υ_* have values ∼15 per cent larger than SPIDER-based results (e.g. Tortora et al. 2013).

As noted by Cappellari et al. (2012), a $\delta_{\rm IMF}$ larger than one can be due to either a bottom-heavy IMF (because of the large fraction of dwarf relative to giant stars) or a top-heavy distribution (because of the large fraction of stellar remnants from evolved massive stars). The degeneracy can be broken by studying gravity-sensitive features in the integrated light of ETGs (Conroy & van Dokkum 2012). These features allow one to constrain the mass fraction of dwarf-to-giant stars in the IMF, rather than the IMF normalization itself (La Barbera et al. 2013), with several studies having found evidence for a bottom-heavier than Chabrier IMF, in high- relative to low-σ ETGs (Ferreras et al. 2013; Spiniello et al. 2014). As shown in Fig. 1, at large $R_{\rm e}$ and $\sigma_{\rm e}$, our results are consistent with the IMF normalization expected for a Salpeter IMF, or even a bottom-heavier than Salpeter IMF.

These results extend our previous analysis in Tortora et al. (2013), in that we explore here a larger set of DM models (i.e. Burkert and 'high-concentration' NFW models), and present also the correlations of $\delta_{\rm IMF}$ with $R_{\rm e}$, n, and mass (besides that with σ), and are consistent with a plethora of independent results from dynamical and stellar population studies (Treu et al. 2010; Thomas et al. 2011; Conroy & van Dokkum 2012; Cappellari et al. 2012, 2013b; Spiniello et al. 2012; Wegner et al. 2012; Dutton et al. 2013; Ferreras et al. 2013; Goudfrooij & Kruijssen 2013, 2014; La Barbera et al. 2013; Tortora et al. 2013, 2014; Weidner et al. 2013; Shu et al. 2014). We notice that for 'high-concentration' NFW models, the best-fitting Υ_* is significantly lower (by ∼0.5 dex, at $\sigma_{\rm e}$ ∼100 km s^{-1}) than that for a Chabrier IMF (i.e. $\delta_{\rm IMF} < 1$). Since the Chabrier IMF gives a minimum normalization with respect to either top- or bottom-heavier distributions (see above), our data seem to be more consistent with a somewhat lower concentration than that

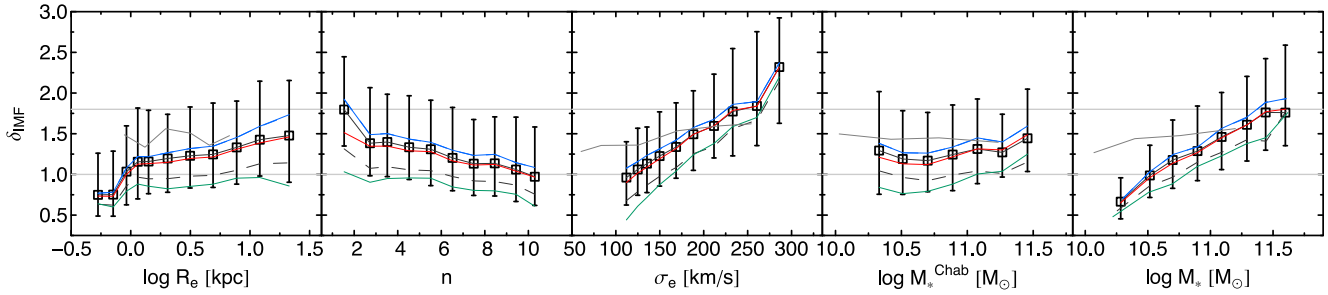

Figure 1. IMF mismatch parameter, $\delta_{\rm IMF}$, for our sample of SPIDER ETGs, as a function of (from left to right) $R_{\rm e}$, n, $\sigma_{\rm e}$, $M_{\star}^{\rm Chab}$ (estimated for a Chabrier IMF), and $M_{\star}$ (allowing for a variable IMF normalization). Open squares and error bars are median and 16–84th percentile trends for our fiducial NFW+Sérsic galaxy model. We also plot results for NFW models with fixed $M_{\rm vir} = 10^{13}\,M_{\rm vir}$ (red curve), 'high-concentration' NFW models (green), contracted NFW models (dashed black line), and Burkert profiles with $r_{\rm B} = 1$ kpc (solid blue line). Note that results for Burkert models with $r_{\rm B} = 20$ kpc are not shown in the plot, as the corresponding trends are identical to the case for $r_{\rm B} = 1$ kpc. The results for ATLAS$^{\rm 3D}$ using the fiducial NFW+Sérsic galaxy model are plotted as dark grey lines. Light grey horizontal lines mark the $\delta_{\rm IMF}$ values expected for a Chabrier ($\delta_{\rm IMF} = 1$) and Salpeter ($\delta_{\rm IMF} \sim 1.8$) IMF.

of the LFS12 $c_{\rm vir}$–$M_{\rm vir}$ relation (see Section 3), although measurement uncertainties on $c_{\rm vir}$ and $\Upsilon_*^{\rm Chab}$ might indeed be responsible for the low (<1) $\delta_{\rm IMF}$ values.

5 TOTAL-MASS DENSITY SLOPES

5.1 Correlations with galaxy properties

We start by presenting results for the SPIDER sample, where the stellar mass profiles of ETGs are characterized with Sérsic fits of NIR (*K*-band) galaxy images (see Section 2.1). In this section, we focus the discussion on results for our reference NFW model, comparing those for different models in Section 5.2. Fig. 2 shows the correlations of logarithmic mass slopes, $\alpha_{\rm l}(R_{\rm e}/2)$ (top) and $\alpha_{\rm l}(R_{\rm e})$ (bottom), as a function of $R_{\rm e}$, Sérsic n, $\sigma_{\rm e}$, and stellar mass (using either a Chabrier IMF, or the IMF normalization provided by our best-fitting model for each galaxy). The $\sigma_{\rm e}$ is the SDSS-fibre velocity dispersion, $\sigma_{\rm Ap}$, corrected to an aperture of one $R_{\rm e}$, following Cappellari et al. (2006). Fig. 3 shows the same correlations as in Fig. 2 but for the mass-weighted (rather than local) slope, $\alpha_{\rm mw}(R_{\rm e})$. Comparing the figures, one can see that the slope value depends significantly on its definition, i.e. $\alpha_{\rm l}(R_{\rm e}/2) \neq \alpha_{\rm l}(R_{\rm e}) \neq \alpha_{\rm mw}(R_{\rm e})$ within the uncertainties, suggesting that either the total mass profile of ETGs is not exactly a power law, or the explored set of models – which are non-power-laws by construction – is not able to describe accurately a power-law behaviour of the profiles (see Section 3.2). More (spatially extended) kinematical data would be necessary to address this issue.

In Tables 1, 2, and 3, we show the results of fitting the trends in Figs 2 and 3, with second-order polynomials of the form $\alpha = a + bx + cx^2$. Errors on slopes are computed by a bootstrap method, and are quoted at the 1σ level. Almost all the correlations are significant at more than 99 per cent.

For our reference, NFW, DM models (solid black curves in the figures), the $\alpha_{\rm l}$ becomes shallower with galaxy mass and radius, reaching, for the highest radii probed, a value of about -1.5, i.e. even shallower than the isothermal value (-2). Milder trends of $\alpha_{\rm l}$, than those for $R_{\rm e}$ and mass, are observed with respect to Sérsic n and $\sigma_{\rm e}$. At $R_{\rm e}/2$, the $\alpha_{\rm l}$ exhibits a double-value behaviour as a function of n, increasing at both high and low n, while $\alpha_{\rm l}(R_{\rm e})$ tends to steepen with n. In terms of $\sigma_{\rm e}$, both $\alpha_{\rm l}(R_{\rm e}/2)$ and $\alpha_{\rm l}(R_{\rm e})$ tend to steepen with velocity dispersion. For $\alpha_{\rm mw}(R_{\rm e})$, as it might be expected, the trends are intermediate between those for $\alpha_{\rm l}(R_{\rm e}/2)$ and $\alpha_{\rm l}(R_{\rm e})$. In general, $\alpha_{\rm mw}(R_{\rm e})$ increases with mass and radius, while it exhibits a double-value behaviour with n, and mildly decreases with $\sigma_{\rm e}$, consistent with the findings for $\alpha_{\rm l}(R_{\rm e}/2)$ and $\alpha_{\rm l}(R_{\rm e})$.

Figs 2 and 3 also plot the slopes of the stellar mass profile only (shaded regions), obtained from the best-fitting *K*-band Sérsic profiles, under the assumption of a radially constant (stellar) M/L (see Section 3). In contrast to $\alpha_{\rm l}$, the stellar mass slope does not vary significantly with $R_{\rm e}$ and $M_\star$. No significant variation with $\sigma_{\rm e}$ is observed (similar to $\alpha_{\rm l}$), while the stellar mass slope tends to steepen with n, as expected by the fact that as n increases, the shape of the Sérsic law becomes more peaked towards the centre. Interestingly, at low $R_{\rm e}$ and $M_\star$, the NFW-based total-mass density slope approaches the slope of the stellar mass component, i.e. that for a constant-M/L profile. This is due to the fact that in the centre of low-mass (small) ETGs, the stellar mass distribution dominates the total mass budget. Note that Tortora et al. (2009b) reached a similar conclusion by comparing central DM density estimates with predictions of ΛCDM toy-models.

For the ATLAS$^{\rm 3D}$ sample, we get, in general, consistent results with those for the SPIDER sample. Fig. 4 (left-hand panel) compares, for example, the trends of $\alpha_{\rm l}(R_{\rm e})$ with $M_\star$ for both samples. The best-fitting trend for SPIDER shown in Table 2 is $\alpha_{\rm l}(R_{\rm e}) = -1.88 + 0.87M_\star - 0.04{M_\star}^2$ with scatter of rms = 0.303, while for ATLAS$^{\rm 3D}$, we find $\alpha_{\rm l}(R_{\rm e}) = -2.23 + 0.68M_\star + 0.69{M_\star}^2$ and a scatter of rms = 0.207. We remark that SPIDER and ATLAS$^{\rm 3D}$ ETGs are analysed here with the same approach, although the galaxy light distributions and stellar masses are characterized in significantly different ways. In fact, the $n = 4$ light profiles for ATLAS$^{\rm 3D}$ galaxies have shallower slopes with respect to the

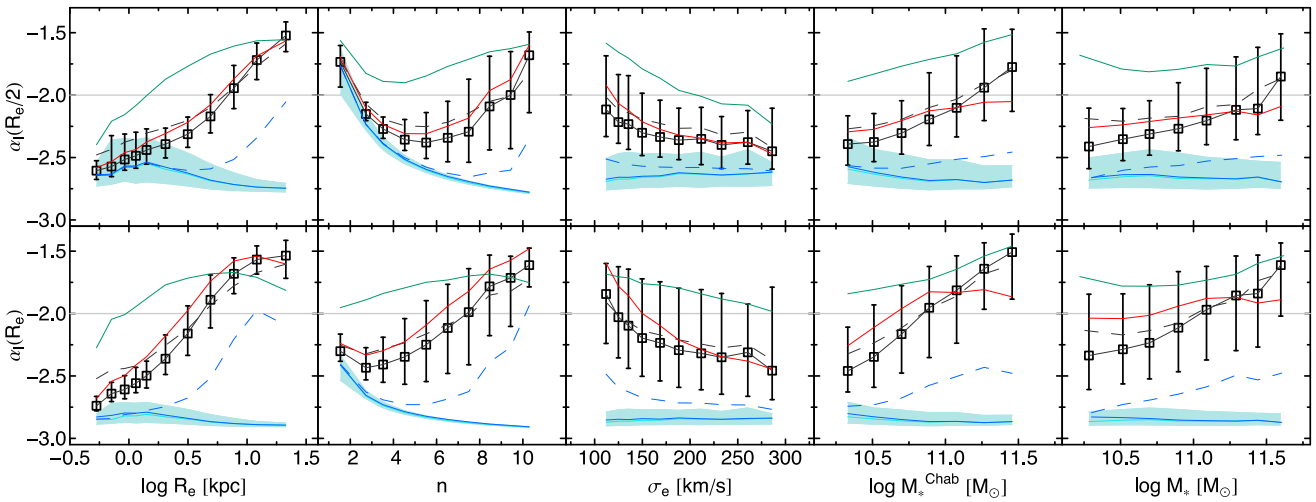

Figure 2. Mass density slopes, for our sample of SPIDER ETGs, as a function of (from left to right) $R_{\rm e}$, n, $\sigma_{\rm e}$, $M_\star^{\rm Chab}$ (Chabrier-IMF stellar mass) and $M_\star$ (stellar mass estimated allowing for a variable IMF normalization). Top and bottom panels refer to the logarithmic density slopes, $\alpha_{\rm l}(R_{\rm e}/2)$ and $\alpha_{\rm l}(R_{\rm e})$, respectively. All slope values are for models with variable Υ_*. Symbols are as in Fig. 1. Results for Burkert profile with $r_{\rm B} = 1$ and 20 kpc are plotted as solid blue and dashed blue lines, respectively. The cyan line and shaded regions mark median and 16–84th percentile slopes for the stellar mass distribution only. In all panels, the grey horizontal line marks the slope value of -2, corresponding to the case of an isothermal sphere.

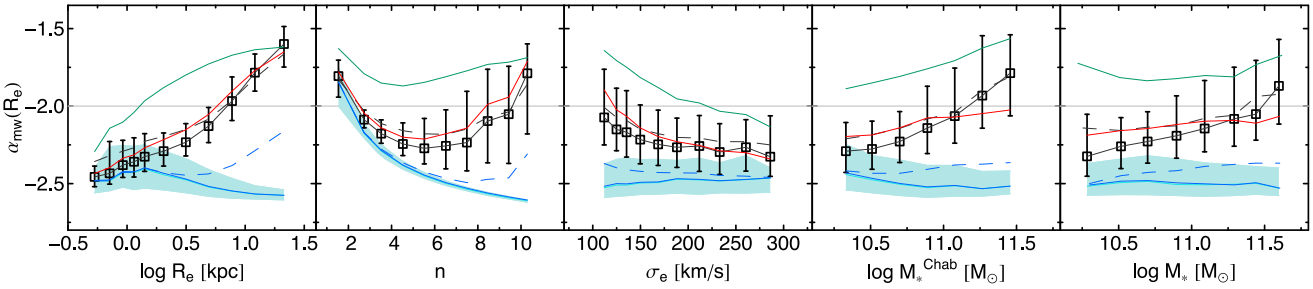

Figure 3. The same as Fig. 2, but for the mass-weighted density slope $\alpha_{mw}(R_e)$.

Table 1. Best-fitting parameters with 1σ errors for the relation $\alpha_l(R_e/2) = a + bx + cx^2$, where $x = \log R_e/3\,\mathrm{kpc}$, $n/4$, $\sigma_e/200\,\mathrm{km\,s^{-1}}$, $\log M_\star^{Chab}/(10^{11}M_\odot)$, and $\log M_\star/(10^{11}M_\odot)$. The scatter (rms) around the best-fitting relation is also reported.

Model		Best fit				
		$\alpha-R_e$	$\alpha-n$	$\alpha-\sigma_e$	$\alpha-M_\star^{Chab}$	$\alpha-M_\star$
	a	-2.288 ± 0.005	-1.28 ± 0.06	-1.66 ± 0.13	-2.14 ± 0.01	-2.23 ± 0.01
NFW+light	b	0.65 ± 0.01	-1.54 ± 0.08	-1.13 ± 0.32	0.63 ± 0.06	0.35 ± 0.03
	c	0.33 ± 0.02	0.54 ± 0.03	0.42 ± 0.18	0.35 ± 0.09	0.13 ± 0.05
	rms	0.148	0.261	0.274	0.255	0.274
	a	-2.20 ± 0.01	-1.29 ± 0.04	-1.11 ± 0.10	-2.12 ± 0.01	-2.17 ± 0.01
NFW ($M_{vir} = 10^{13}\,M_\odot$)	b	0.64 ± 0.01	-1.48 ± 0.07	-1.97 ± 0.24	0.21 ± 0.04	0.11 ± 0.02
	c	0.17 ± 0.02	0.53 ± 0.02	0.73 ± 0.13	-0.10 ± 0.08	-0.03 ± 0.05
	rms	0.192	0.263	0.241	0.293	0.301
	a	-2.19 ± 0.01	-1.43 ± 0.03	-1.62 ± 0.10	-2.07 ± 0.01	-2.14 ± 0.01
NFW+AC	b	0.51 ± 0.01	-1.11 ± 0.06	-0.96 ± 0.23	0.47 ± 0.03	0.25 ± 0.03
	c	0.22 ± 0.02	0.38 ± 0.02	0.31 ± 0.13	0.25 ± 0.07	0.26 ± 0.05
	rms	0.138	0.217	0.214	0.205	0.226
	a	-2.59 ± 0.01	-1.29 ± 0.04	-2.34 ± 0.08	-2.54 ± 0.005	-2.539 ± 0.004
Burkert ($r_B = 20\,kpc$)	b	0.24 ± 0.01	-1.57 ± 0.06	-0.43 ± 0.19	0.13 ± 0.02	0.13 ± 0.01
	c	0.36 ± 0.03	0.44 ± 0.02	0.18 ± 0.11	0.13 ± 0.05	-0.05 ± 0.02
	rms	0.164	0.170	0.192	0.197	0.195
	a	-2.615 ± 0.004	-1.42 ± 0.04	-2.73 ± 0.12	-2.688 ± 0.005	-2.652 ± 0.004
Burkert ($r_B = 1\,kpc$)	b	-0.10 ± 0.01	-1.27 ± 0.05	0.12 ± 0.28	-0.06 ± 0.02	-0.03 ± 0.01
	c	-0.12 ± 0.02	0.30 ± 0.02	-0.03 ± 0.15	0.16 ± 0.04	-0.04 ± 0.02
	rms	0.152	0.055	0.155	0.152	0.158
	a	-1.776 ± 0.005	-1.51 ± 0.03	-0.89 ± 0.17	-1.68 ± 0.01	-1.8 ± 0.01
NFW (LFS $c_{vir}-M_{vir}$)	b	0.55 ± 0.02	-0.51 ± 0.05	-1.48 ± 0.40	0.32 ± 0.05	0.08 ± 0.02
	c	-0.35 ± 0.03	0.19 ± 0.02	0.40 ± 0.22	0.02 ± 0.09	0.29 ± 0.04
	rms	0.190	0.239	0.200	0.243	0.253
	a	-2.624 ± 0.005	-1.43 ± 0.04	-2.78 ± 0.09	-2.692 ± 0.005	-2.66 ± 0.01
Sérsic light	b	-0.09 ± 0.01	-1.27 ± 0.05	0.19 ± 0.23	-0.05 ± 0.02	-0.01 ± 0.01
	c	-0.11 ± 0.02	0.3 ± 0.02	-0.06 ± 0.13	0.15 ± 0.04	-0.05 ± 0.02
	rms	0.141	0.055	0.158	0.152	0.158

SPIDER Sérsic laws.[4] The agreement between the two data sets is good, although the trend with mass for ATLAS^{3D} tends to be shallower than that for SPIDER, with steeper slopes at high masses, because of the shallower (de Vaucouleurs versus Sérsic) light profile. At the lowest $M_\star$ ($\sim 10^{10}\,M_\odot$), which can be probed only with ATLAS^{3D}, one can observe an inversion of the mass density trend with the slope, with α_l becoming shallower than at $M_\star \sim 10^{10.5}\,M_\odot$. However, this result might be just reflecting the fact that the $r^{1/4}$ law is not very accurate for low- relative to high-mass ETGs. The right-hand panel of Fig. 4 also shows the correlation of mass density slopes with central DM fraction within R_e $f_{DM}(R_e)$. As for best fits in Tables 1, 2, and 3, the trend is quite well fitted by a polynomial. We find $\alpha_l(R_e) = -2.65 + 3.42x - 2.52x^2$, with $x = f_{DM}(R_e)$ and a scatter of 0.07. For ATLAS^{3D}, the fit is $\alpha_l(R_e) = -2.73 + 3.91x - 3.94x^2$ with the same scatter found for SPIDER sample. We find consistent results between the two data sets, with shallower density profiles in galaxies that are more DM dominated in the centre, consistent with independent results from Auger et al. (2010) and Dutton & Treu (2014, see below).

Fig. 4 also compares the SPIDER and ATLAS^{3D} trends with those obtained for SPIDER ETGs, by computing density mass slopes and DM fractions with $r^{1/4}$ (i.e. de Vaucouleurs) structural parameters in r band from SDSS-DR6, rather than Sérsic 2DPHOT parameters in K band (see La Barbera et al. 2010 for details). This comparison allows us to single out the effect of differences due to light profile shape, from those of different wavebands and

[4] Cappellari et al. (2013a) found that stellar light profiles were well fitted by an isothermal law within 1 R_e (see their fig. 2). Our stellar-light slopes for the ATLAS^{3D} galaxies would be consistent with their findings if the same slope definition were adopted.

Table 2. Best-fitting parameters with 1σ errors for the relation $\alpha_1(R_e) = a + bx + cx^2$, where $x = \log R_e/3\,\mathrm{kpc}$, $n/4$, $\sigma_e/200\,\mathrm{km\,s^{-1}}$, $\log M_\star{}^{\mathrm{Chab}}/(10^{11}\mathrm{M}_\odot)$, and $\log M_\star/(10^{11}\mathrm{M}_\odot)$. The scatter (rms) around the best-fitting relation is also reported.

Model		Best fit				
		$\alpha-R_e$	$\alpha-n$	$\alpha-\sigma_e$	$\alpha-M_\star{}^{\mathrm{Chab}}$	$\alpha-M_\star$
	a	-2.141 ± 0.005	-2.33 ± 0.03	-1.02 ± 0.24	-1.88 ± 0.02	-2.06 ± 0.01
NFW+light	b	0.86 ± 0.01	-0.21 ± 0.05	-2.05 ± 0.54	0.87 ± 0.03	0.57 ± 0.02
	c	-0.03 ± 0.02	0.2 ± 0.01	0.75 ± 0.30	-0.04 ± 0.07	0.23 ± 0.07
	rms	0.170	0.292	0.341	0.303	0.339
	a	-1.97 ± 0.01	-2.34 ± 0.04	-0.28 ± 0.18	-1.82 ± 0.02	-1.93 ± 0.02
NFW ($M_{\mathrm{vir}} = 10^{13}\,\mathrm{M}_\odot$)	b	0.81 ± 0.01	-0.01 ± 0.05	-3.04 ± 0.43	0.21 ± 0.04	0.14 ± 0.03
	c	-0.31 ± 0.02	0.14 ± 0.02	1.07 ± 0.23	-0.68 ± 0.13	-0.08 ± 0.09
	rms	0.224	0.285	0.292	0.348	0.359
	a	-2.11 ± 0.01	-2.29 ± 0.03	-1.37 ± 0.13	-1.90 ± 0.01	-2.03 ± 0.01
NFW+AC	b	0.64 ± 0.01	-0.07 ± 0.04	-1.29 ± 0.31	0.68 ± 0.03	0.43 ± 0.02
	c	0.04 ± 0.03	0.12 ± 0.02	0.42 ± 0.16	0.05 ± 0.07	0.37 ± 0.05
	rms	0.158	0.241	0.268	0.237	0.272
	a	-2.6 ± 0.01	-2.05 ± 0.03	-2.10 ± 0.09	-2.55 ± 0.01	-2.61 ± 0.01
Burkert ($r_B = 20\,\mathrm{kpc}$)	b	0.56 ± 0.01	-1.12 ± 0.05	-1.03 ± 0.21	0.28 ± 0.02	0.26 ± 0.02
	c	0.25 ± 0.03	0.44 ± 0.02	0.41 ± 0.10	-0.09 ± 0.05	-0.002 ± 0.032
	rms	0.205	0.265	0.305	0.311	0.321
	a	-2.832 ± 0.001	-2.24 ± 0.02	-2.87 ± 0.05	-2.868 ± 0.002	-2.854 ± 0.001
Burkert ($r_B = 1\,\mathrm{kpc}$)	b	-0.062 ± 0.003	-0.64 ± 0.03	0.03 ± 0.11	-0.04 ± 0.01	-0.029 ± 0.005
	c	-0.037 ± 0.005	0.15 ± 0.01	-0.01 ± 0.06	0.09 ± 0.02	0.02 ± 0.01
	rms	0.063	0.032	0.071	0.071	0.071
	a	-1.716 ± 0.007	-2.1 ± 0.04	-1.64 ± 0.27	-1.673 ± 0.005	-1.76 ± 0.01
NFW (LFS $c_{\mathrm{vir}}-M_{\mathrm{vir}}$)	b	0.32 ± 0.02	0.38 ± 0.06	0.04 ± 0.66	0.38 ± 0.02	0.19 ± 0.02
	c	-0.5 ± 0.04	-0.09 ± 0.02	-0.22 ± 0.38	0.21 ± 0.05	0.34 ± 0.03
	rms	0.173	0.195	0.192	0.184	0.214
	a	-2.841 ± 0.002	-2.25 ± 0.02	-2.91 ± 0.05	-2.871 ± 0.002	-2.856 ± 0.002
Sérsic light	b	-0.041 ± 0.005	-0.64 ± 0.03	0.08 ± 0.11	-0.02 ± 0.01	-0.01 ± 0.01
	c	-0.05 ± 0.01	0.15 ± 0.01	-0.02 ± 0.06	0.066 ± 0.02	-0.02 ± 0.01
	rms	0.063	0.032	0.071	0.071	0.071

sample selection, on the observed trends. The $r^{1/4}$ trends with $M_\star$ are shallower than reference ones for SPIDER, and fairly consistent with those for ATLAS^{3D}, the small difference between solid (ATLAS^{3D}) and dashed (SPIDER $r^{1/4}$) grey curves being likely explained by differences in sample selection. The fact that $r^{1/4}$, with respect to Sérsic, parameters provide steeper density slopes is also consistent with the trends in the bottom panels of Fig. 2. In fact, fitting a $n = 4$ light profile gives smaller R_e values than those for a Sérsic law, with steepest α values being found for $n \sim 4$ and the smallest R_e.

5.2 Comparison of different DM models

We discuss here how different assumptions on the DM component affects the trends of the mass density slope. As shown in Figs 2 and 3, the slope values are degenerate with halo model (see also best fits in Tables 1, 2, and 3). For most correlations, the Burkert and 'high-concentration' NFW models (see blue and green curves) provide slope values encompassing the whole range of values for α_1, with the reference NFW model being in between these models (Cardone & Tortora 2010; Cardone et al. 2011b). Note that the estimate of total-mass density slope is deeply related to the best-fitting Υ_*, as for increasing Υ_* the mass budget in the central regions resembles more the one for the light component alone. In fact, contracted halo models, which imply a larger DM content towards the galaxy centre, with smaller Υ_* (see Fig. 1), tend to give shallower slopes than the reference NFW models, with this behaviour being even more pronounced for 'high-concentration' models. On the other hand, Burkert profiles provide steeper slopes, in between those for NFW models and stellar mass density (i.e. constant-M/L) slopes (Tortora et al. 2013). Remarkably, in the case of Burkert models, the slopes show almost constant trends with all galaxy properties, including mass and radius, in sharp contrast with the significant trends obtained for all other models. In particular, the results for the model with $r_B = 1$ kpc closely resemble the slopes of the stellar mass distribution. Note that, different than for NFW models, we have not adopted a trend of core radius with galaxy mass (equivalent to an M_{vir}–$M_\star$ relation) for Burkert models, but just two reference values of $r_B = 1$ and 20 kpc. These values approximately bracket the results found for two elliptical galaxies by MSB11 and the range of core radii obtained by Thomas et al. (2009) using cored logarithmic haloes, which resemble Burkert profiles in the galactic centres. Thus, using a radius–mass relation would not change significantly our results for the Burkert profiles.

Note that NFW models with fixed virial mass and concentration (red curves in the figures) give shallower slopes than, but similar trends to, the NFW case. In some cases, the slopes are also (marginally) shallower than those for NFW-contracted profiles. For 'high-concentration' models, the trends deviate significantly – with higher (i.e. shallower) α values – from our reference model. This is more pronounced at low- relative to high mass, making the trends of α with mass significantly shallower than for reference models. On the other hand, the trends with radius and σ_e are more robust to the c_{vir}–M_{vir} prescription, in particular for $\alpha_1(R_e/2)$.

In summary, we find that the strong increase of the mass density slope with galaxy radius, as well as the decrease with σ_e, are robust findings against different ingredients of NFW halo models. The trend with mass is less robust, in that it is significantly shallower

Table 3. Best-fitting parameters with 1σ errors for the relation $\alpha_{\rm mw}(R_{\rm e}) = a + bx + cx^2$, where $x = \log R_{\rm e}/3\,{\rm kpc}$, $n/4$, $\sigma_{\rm e}/200\,{\rm km\,s^{-1}}$, $\log M_\star{}^{\rm Chab}/(10^{11}{\rm M}_\odot)$, and $\log M_\star/(10^{11}{\rm M}_\odot)$. The rms is also reported. The scatter (rms) around the best-fitting relation is also reported.

Model		Best fit				
		$\alpha-R_{\rm e}$	$\alpha-n$	$\alpha-\sigma_{\rm e}$	$\alpha-M_\star{}^{\rm Chab}$	$\alpha-M_\star$
NFW	a	-2.218 ± 0.004	-1.47 ± 0.04	-1.73 ± 0.09	-2.1 ± 0.01	-2.16 ± 0.01
	b	0.50 ± 0.01	-1.12 ± 0.06	-0.85 ± 0.2	0.51 ± 0.3	0.28 ± 0.02
	c	0.28 ± 0.01	0.38 ± 0.02	0.31 ± 0.10	0.35 ± 0.06	0.09 ± 0.04
	rms	0.122	0.212	0.212	0.195	0.210
NFW ($M_{\rm vir} = 10^{13}\,{\rm M}_\odot$)	a	-2.139 ± 0.005	-1.45 ± 0.04	-1.24 ± 0.09	-2.08 ± 0.01	-2.11 ± 0.01
	b	0.48 ± 0.01	-1.08 ± 0.06	-1.62 ± 0.19	0.14 ± 0.03	0.07 ± 0.02
	c	0.13 ± 0.02	0.38 ± 0.02	0.61 ± 0.10	-0.08 ± 0.06	-0.07 ± 0.04
	rms	0.161	0.217	0.184	0.235	0.239
NFW+AC	a	-2.147 ± 0.005	-1.57 ± 0.03	-1.62 ± 0.13	-2.05 ± 0.01	-2.11 ± 0.01
	b	0.40 ± 0.01	-0.83 ± 0.04	-0.93 ± 0.32	0.41 ± 0.04	0.21 ± 0.02
	c	0.20 ± 0.02	0.27 ± 0.01	0.35 ± 0.18	0.25 ± 0.08	0.23 ± 0.03
	rms	0.130	0.190	0.184	0.176	0.192
Burkert ($r_{\rm B} = 20\,{\rm kpc}$)	a	-2.431 ± 0.004	-1.51 ± 0.02	-2.25 ± 0.08	-2.401 ± 0.004	-2.398 ± 0.004
	b	0.13 ± 0.01	-1.1 ± 0.04	-0.31 ± 0.19	0.07 ± 0.01	0.09 ± 0.01
	c	0.16 ± 0.02	0.30 ± 0.01	0.13 ± 0.11	0.05 ± 0.03	-0.07 ± 0.01
	rms	0.122	0.105	0.130	0.134	0.134
Burkert ($r_{\rm B} = 1\,{\rm kpc}$)	a	-2.463 ± 0.004	-1.58 ± 0.02	-2.58 ± 0.09	-2.524 ± 0.004	-2.49 ± 0.01
	b	-0.09 ± 0.01	-0.92 ± 0.03	0.17 ± 0.22	-0.05 ± 0.02	-0.02 ± 0.01
	c	-0.1 ± 0.01	0.21 ± 0.01	-0.05 ± 0.13	0.14 ± 0.04	-0.05 ± 0.02
	rms	0.110	0.032	0.126	0.118	0.126
NFW (LFS $c_{\rm vir}-M_{\rm vir}$)	a	-1.804 ± 0.004	-1.55 ± 0.03	-1.06 ± 0.12	-1.72 ± 0.01	-1.83 ± 0.01
	b	0.44 ± 0.01	-0.42 ± 0.04	-1.29 ± 0.28	0.29 ± 0.04	0.08 ± 0.02
	c	-0.27 ± 0.02	0.15 ± 0.01	0.39 ± 0.16	0.07 ± 0.08	0.27 ± 0.03
	rms	0.164	0.205	0.164	0.20	0.210
Sérsic light	a	-2.469 ± 0.004	-1.60 ± 0.02	-2.60 ± 0.08	-2.53 ± 0.004	-2.497 ± 0.003
	b	-0.08 ± 0.01	-0.90 ± 0.03	0.18 ± 0.20	-0.04 ± 0.02	-0.01 ± 0.01
	c	-0.09 ± 0.01	0.2 ± 0.01	-0.06 ± 0.12	0.14 ± 0.04	-0.04 ± 0.02
	rms	0.114	0.032	0.126	0.122	0.126

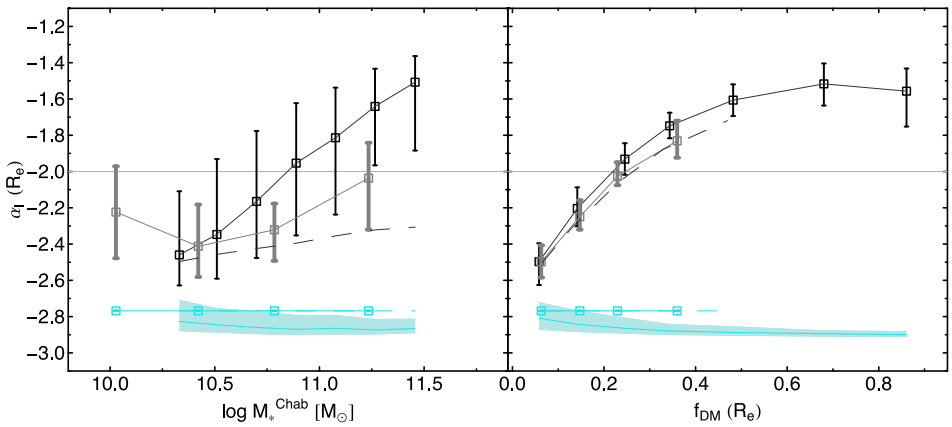

Figure 4. Comparison of trends of mass density slope, $\alpha_{\rm I}(R_{\rm e})$, with $M_\star$ (left) and DM fraction, $f_{\rm DM}(R_{\rm e})$ (right), between SPIDER (black squares) and ATLAS$^{\rm 3D}$ (grey squares) samples. Error bars mark the 16–84th percentile scatter intervals on the slopes. Cyan shaded regions and squares mark the stellar mass slopes, at one $R_{\rm e}$, for SPIDER and ATLAS$^{\rm 3D}$, respectively. Note that for ATLAS$^{\rm 3D}$, the slope of the light distribution is constant, as the light profile is parametrized by a (fixed-shape) de Vaucouleurs model. As a comparison, we also plot, as dashed curves, the trends obtained for SPIDER ETGs when using SDSS-DR6 *r*-band de Vaucouleurs (rather than *K*-band Sérsic) models to parametrize the galaxy light profiles (dashed lines).

for 'high-concentration' models. However, as noticed in Section 4, the 'high-concentration' models provide overly low IMF normalizations at low galaxy mass (i.e. lower than those measured for a Chabrier IMF), which might favour (somewhat) lower concentration profiles. Moreover, one can notice that the $c_{\rm vir}$–$M_{\rm vir}$ relation from LFS12 is derived by assuming a fixed Chabrier IMF. Although this might be important at high galaxy mass, where the IMF normalization is found to be larger than the Chabrier one (e.g. Tortora et al. 2013, and Fig. 1), we find fair agreement, at high radius/large mass, between density slopes for fiducial NFW and

'high-concentration' models. In contrast, all correlations tend to be washed out when using Burkert profiles. However, such models, while reproducing quite well the dynamics of dwarf galaxies and spirals, likely provide too *light* haloes in massive ETGs (Cardone & Tortora 2010), with respect to many results pointing to a significant amount of DM at the virial radius in these systems (e.g. Benson et al. 2000; Marinoni & Hudson 2002; van den Bosch et al. 2007; Moster et al. 2010). Therefore, while we have included here also Burkert models in the analysis, these should be considered as rather unlikely for the most massive galaxies in our samples.

5.3 Impact of different assumptions

Our dynamical approach relies on several assumptions, i.e. (i) spherical symmetry, (ii) isotropy, (iii) no stellar M/L-gradients within a galaxy, and (iv) no significant rotation. We have performed a variety of tests, showing that these assumptions do not affect significantly the correlations of mass density slope with galaxy properties.

(i) In general, for a flattened system, the use of spherical models tends to over (under)estimate the inferred galaxy mass, if the system is seen edge-on (face-on). To minimize the fraction of non-spherical systems (e.g. S0's), for both SPIDER and ATLAS^{3D} samples, we have restricted the analysis to 'round' objects, with axis ratio $q > 0.8$. We found that the slope trends remain unchanged, within a few per cent, with respect to those for the entire samples.

(ii) To explore the effect of radial anisotropy, we have adopted two empirically motivated values of the radial anisotropy parameter, $\beta = +0.1$ and $+0.2$, respectively (Gerhard et al. 2001). For $\beta > 0$, the model velocity dispersion at a given radius is larger than for $\beta = 0$, with the net effect of reducing our inferred masses within that radius. For $\beta = +0.1$ and $+0.2$, the inferred masses at 1 R_e were found to change by $\sim$2 and 4 per cent, respectively, with negligible impact on the mass density slopes, considering the observed scatter of slope values.

(iii) Radial gradients of M/L can also affect our density slope estimates. However, at optical wavebands, such gradients are very mild in massive ETGs (Tortora et al. 2011), and are expected to be even smaller in the NIR, where most of the integrated light from a stellar population is dominated by its old quiescent component. Indeed, the fact that for r-(ATLAS^{3D}) and K-(SPIDER)band data, we find consistent slope estimates, indicates that M/L gradients are not important for our analysis.

(iv) The ATLAS^{3D} sample gives us the opportunity to test the impact of neglecting rotational velocity and galaxy flattening in our analysis. From best-fitting Jeans anisotropic MGE (JAM) models, the ATLAS^{3D} team obtained the best-fitting relation $V_{\rm circ}^{\rm obs}(R_{\rm e,maj}) \approx 1.51 \times \sigma_e$, where $V_{\rm circ}$ is the model circular velocity and $R_{\rm e,\,maj}$ is the effective radius along the galaxy major axis (Cappellari et al. 2013a). Using the expression $V_{\rm circ}^{\rm theo} \equiv \sqrt{GM_{\rm dyn}/r}$, we have converted the $V_{\rm circ}^{\rm obs}(R_{\rm e,maj})$ from ATLAS^{3D} to a dynamical mass, $M_{\rm dyn}$. Even in this case, we found that neglecting rotation has negligible effects, within a few per cent, on the mass density slopes.

6 COMPARISON WITH LITERATURE

6.1 Observations

Fig. 5 compares some of our findings with independent estimates of the mass density slope from the literature. At the highest mass scales probed in this work, our results are consistent with Auger et al. (2010), who fitted a sample of SLACS lenses, at intermediate redshifts, with a power-law mass density profile, $\rho(r) \propto r^{\alpha}$, combining gravitational lensing and central dynamics to probe the total mass distribution at $R_e/2$. They found the mass distribution to be well described by an isothermal profile (Treu & Koopmans 2004; Gavazzi et al. 2007; Auger et al. 2010). The average slope value from Auger et al. (2010) is plotted in the top panels of Fig. 5 (see red squares and error bars), versus $M_\star$ (left) and $f_{\rm DM}(R_e/2)$ (right), respectively. Note that Auger et al. (2010) derived stellar masses by assuming a Salpeter IMF. Therefore, to perform a meaningful comparison, we also converted our Chabrier-IMF $M_\star$'s into Salpeter-IMF stellar masses, accounting for the different overall normalizations of the Chabrier and Salpeter IMFs.

The agreement between Auger et al. (2010) – who estimated the density slope of massive early-type lenses – and our most massive bin for fiducial NFW models, is excellent, with a good agreement also with respect to $f_{\rm DM}$. The best-fitting relation $\alpha_{\rm l}(R_e/2)$–$M_\star^{\rm Chab}$ shown in Table 1, because of the change of IMF, is now $\alpha_{\rm l}(R_e/2) = -2.28 + 0.40x + 0.40x^2$, with $x = M_\star^{\rm Salp}$ and a scatter of rms $= 0.255$. The trend with $f_{\rm DM}$ is best fitted by the polynomial $\alpha_{\rm l}(R_e/2) = -2.49 + 2.86x - 1.91x^2$, with $x = f_{\rm DM}(R_e/2)$ and a scatter of rms $= 0.130$.

However, Auger et al. (2010) assumed a fixed, Salpeter, IMF, while our dynamical approach leaves the IMF normalization – through the best-fitting stellar mass-to-light ratio – as a free model parameter. To test the effect of IMF normalization, we have selected only galaxies in our sample that are best described by a Salpeter-like normalization (with $1.6 < \delta_{\rm IMF} < 2$). This selection leads to mild variations (<10 per cent) in the slope trends at high galaxy mass (see purple curves in the figure), with slopes still in excellent agreement with SLACS. The agreement is good also when we compare the trends with R_e and velocity dispersion with ours in the top panels in Fig. 2, as Auger et al. (2010) find shallower slopes at larger R_e and an almost constant trend with velocity dispersion.

Fig. 5 also shows that Burkert profiles (dashed and solid blue curves in the top panels) give slopes that are too steep (at the 2.5σ level) with respect to SLACS. Thus, the comparison of our dynamical analysis with gravitational lensing results at intermediate redshift seems to reject Burkert profiles as plausible models to describe the DM component of (massive) ETGs, while it is fully consistent with massive ETGs having an isothermal total-mass density profile.

In the bottom panels of Fig. 5, we compare our findings, in terms of $\alpha_{\rm mw}(R_e)$, with the dynamical analysis performed for an SDSS sample of ETGs, by Dutton & Treu (2014, hereafter DT14). The $\alpha_{\rm mw}(R_e)$ is plotted versus $M_\star$ (left) and $f_{\rm DM}(R_e)$ (right). The best-fitting relation $\alpha_{\rm l}(R_e/2)$–$M_\star^{\rm Salp}$ is $\alpha_{\rm mw}(R_e) = -2.21 + 0.31x + 0.38x^2$, with $x = M_\star^{\rm Salp}$ and a scatter of rms $= 0.196$. The trend with $f_{\rm DM}$ is best fitted by the polynomial $\alpha_{\rm mw}(R_e) = -2.41 + 1.06x - 0.01x^2$, with $x = f_{\rm DM}(R_e)$ and a scatter of rms $= 0.095$. The authors modelled the galaxy light profiles with the combination of an $n = 1$ and 4 Sérsic law, with a suite of models to describe the DM distribution (including fiducial NFW, constant-M/L, contracted, and expanded models), with varying stellar M/L. The figure compares their findings with ours, for NFW, contracted-NFW, and constant-M/L profiles. In general, the shape of the correlations are similar when comparing ours and DT14 results, but some offsets, at the 10 per cent level, exist. In particular, constant-M/L models from DT14 (magenta curves) have slopes $\sim$8 per cent shallower than ours (cyan curve and shaded region), while mass density slopes for NFW models are steeper (shallower) than ours when plotted with respect to $M_\star$ ($f_{\rm DM}$). A good agreement is found for contracted-NFW models. The offset between our NFW-model slopes and those of DT14 is likely due to

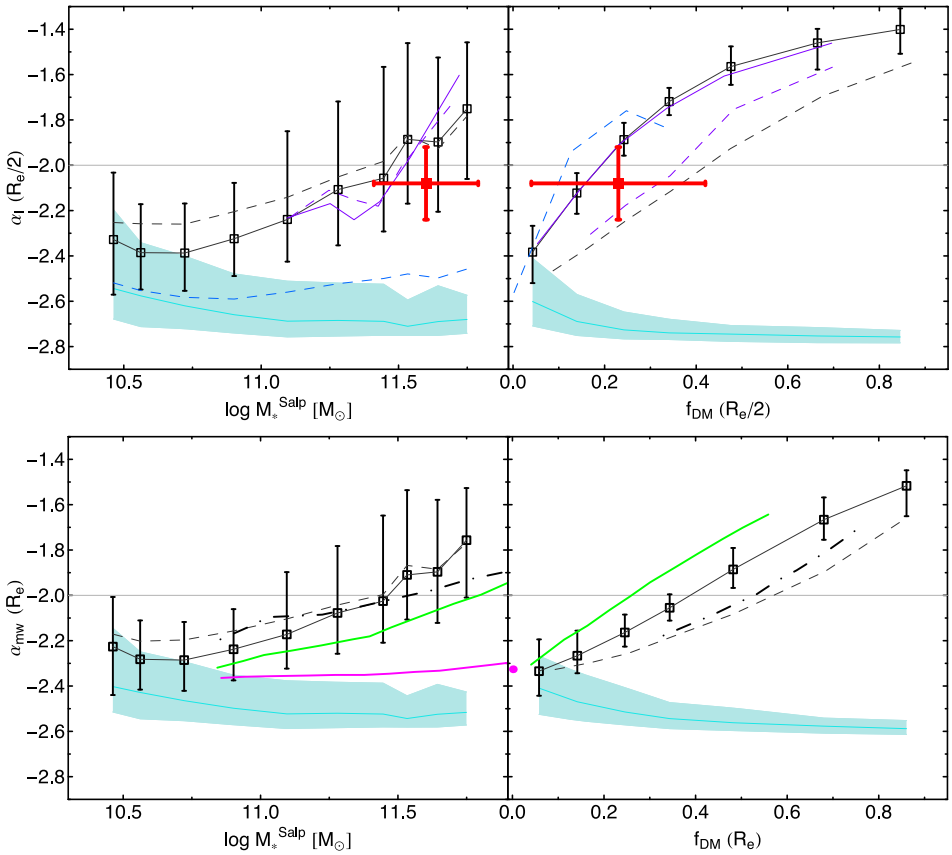

Figure 5. Comparison of total-mass density profile slopes with data from the literature, as a function of $M_\star$ (left-hand panels) and $f_{\rm DM}$ (right-hand panels). Black symbols with error bars and cyan lines and regions are the same as in Figs 2 and 3, plotting the slope trends of SPIDER ETGs, for our fiducial, NFW+Sérsic, model (black curve and error bars) and the slopes for the stellar mass profile only (cyan curve and shaded region), respectively. Top and bottom panels are for $\alpha_{\rm l}(R_{\rm e}/2)$ and $\alpha_{\rm mw}(R_{\rm e})$, respectively. Literature data include: average slope and 1σ scatter for SLACS lenses (Auger et al. 2010), plotted with red squares and error bars in the top panels; slopes obtained for constant-M/L (magenta curves), NFW (green curves), and contracted-NFW (dot dashed black curves) profiles from Dutton & Treu (2014) in the bottom panels. Purple solid and dashed lines in the top panels are the slope trends for SPIDER ETGs with Salpeter IMF normalization (see the text for details).

the different modelling of the galaxy light distribution between our study and theirs. In fact, as shown in Fig. 3, the $\alpha_{\rm mw}(R_{\rm e})$ of SPIDER ETGs with $n \sim 4$ is lower (i.e. steeper) than that for both higher and lower n galaxies, especially for NFW-model slopes, suggesting that a combination of $n = 1$ and 4 Sérsic laws, to model the light distribution of ETGs, can produce lower (steeper) $\alpha_{\rm mw}(R_{\rm e})$ slopes than those for a single Sérsic law with variable n, consistent with what seen in the comparison of DT14 and our trends. A good agreement is found for the trend with $R_{\rm e}$, while DT14 find shallower slopes in high-$\sigma_\star$ galaxies, in agreement with recent findings from gravitational lenses (Shu et al. 2014), but in contrast with our constant trends (see Fig. 3).

The fact that the mass density slope becomes shallower at high-, relative to low-, mass is also consistent with the findings of Humphrey & Buote (2010, hereafter HB10). Using *Chandra* X-ray data, under the assumption of hydrostatic equilibrium, HB10 analysed a sample of 10 systems, spanning $\sim$2 orders of magnitude in $M_{\rm vir}$, from massive galaxies to clusters of galaxies, in the radial range from $\lesssim R_{\rm e}$ to several $R_{\rm e}$'s. They found isothermal profiles for galaxies, consistent with our results for massive ETGs, and shallower than isothermal slopes (up to $\alpha = -1.2$) for galaxy clusters.

6.2 Simulations

We compare our results with predictions for a suite of simulated galaxies, from Remus et al. (2013, hereafter R13). The comparison is shown in Fig. 6, where we plot mass density slopes, for our fiducial (NFW+Sérsic) model, as a function of stellar mass (left) and central DM fraction (right). R13 computed mass density slopes by fitting mass density profiles with a power law, in the radial range 0.3–4 $r_{1/2}$, where $r_{1/2}$ is the half-mass radius of a simulated galaxy. To perform a meaningful comparison, we re-computed our slopes with the same definition as in R13, converting the projected effective radius of a given galaxy into its half-mass (de-projected) radius. We used the relation $R_{\rm e} = r_{1/2}/1.35$, which turns out to be independent of the Sérsic n (see e.g. appendix B of Wolf et al. 2010). We refer to the slopes, defined as in R13, as $\alpha_{\rm av}$.

Fig. 6 plots the $\alpha_{\rm av}$ for all models from R13 (see dots with different colours), except for simulated brigthest cluster galaxies (BCGs), whose mass range is above that covered by our trends. The simulations include several high-resolution 'binary mergers', i.e. (a) spiral–spiral mergers with a progenitor mass ratio 1: 1 (black), (b) spiral–spiral mergers with mass ratio 3: 1 (blue), (c) a mixed merger of a spiral galaxy with an elliptical, the latter formed by a 3:1 spiral–spiral merger (cyan), (d) one spiral–spiral merger, with a

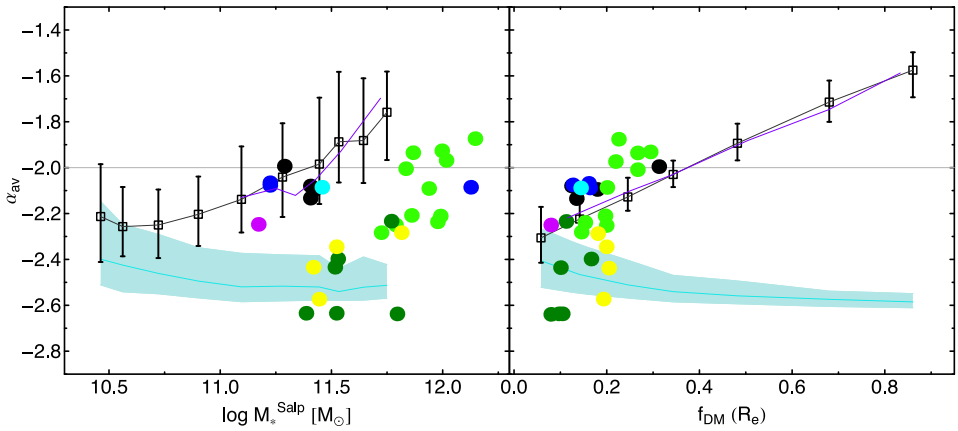

Figure 6. Comparison of total-mass density slope trends with predictions for simulated galaxies from R13. Left- and right-hand panels plot α_{av} versus $M_\star$ and f_{DM} (within 1 R_e), respectively. The slope, α_{av}, is defined by fitting mass density profiles with a power law, in the radial range 0.3–4 $r_{1/2}$, where $r_{1/2}$ is the galaxy half-mass radius (i.e. adopting the same slope definition as in R13, see the text for details). Black symbols with error bars and cyan lines and regions are the same as in Figs 2 and 3. Our stellar masses are re-scaled to a Salpeter IMF, as in R13. Purple lines are the observed trends for the subsample of SPIDER ETGs with Salpeter-like IMF normalization (see Section 6.1). Dots with different colours are simulated galaxies from R13: black, blue, cyan and pink dots correspond to idealized single binary mergers, while light-green, dark-green, and yellow dots are for merging systems drawn from cosmological simulations (see Section 6.2 for details). Note the good agreement of our trends with binary mergers simulations, including also the effect of BH growth and feedback.

mass ratio 3: 1, and a large gas fraction of 80 per cent (pink). Furthermore, we plot 17 simulated elliptical galaxies formed from multiple mergers, in the framework of a cosmological simulation: (e) the most massive merger remnants, re-simulated with twice the spatial resolution of the original DM box (light green), (f) the less massive remnants, re-simulated with four times the original resolution of DM particles (dark green), and (g) four companion ellipticals, which are substructures within larger haloes (yellow). R13 referred to simulations (e–f) as CosmoZoom Ellipticals, and simulations (g) as CosmoZoom Companions. All simulations have been performed by R13 with modified versions of the parallel TreePM-SPH-code GADGET-2, including the effect of star formation and feedback from SNe's, assuming a Salpeter IMF. Black hole (BH) growth and feedback are included in the binary merger simulations only, while CosmoZoom simulations do not include any BH treatment.

Several simulated galaxies (in particular the most massive CosmoZoom Ellipticals) have masses larger than the range covered by our data, hampering a direct comparison to our results. Therefore, we focus the comparison on objects having $\log M_\star/M_\odot \lesssim 11.8$ in Fig. 6. All binary mergers in this mass range are in good agreement with our results in both the α_{av}–$M_\star$ and α_{av}–f_{DM} plots. The same result holds when comparing simulations to the trends for ETGs with a Salpeter-like IMF normalization (see Section 6), i.e. the same IMF as in R13. On the contrary, CosmoZoom galaxies, in the mass range from $\log M_\star/M_\odot \sim 11.3$ to $\log M_\star/M_\odot \sim 11.8$ (green and yellow dots in the figure) have systematically steeper slopes, at a given stellar mass, than our data, which is more consistent with slopes for a constant M/L profile (i.e. the cyan region in the figure). A similar discrepancy exists with respect to f_{DM}, although in the α_{av}–f_{DM} plane, the deviation of CosmoZoom galaxies from our fiducial trends (black curves) is smaller than in the α_{av}–$M_\star$ diagram. This is due to the fact that, at fixed stellar mass, CosmoZoom galaxies also have lower DM fractions than real galaxies.

We argue that the excellent agreement found between our results and the predictions of binary merger simulations can be due to the inclusion of BH feedback in them, which is more efficient than SN feedback in suppressing star formation (Tortora et al. 2009a; Martizzi, Teyssier & Moore 2014), producing less stellar mass in the galaxy centre, and nearly isothermal total mass profiles, in agreement with the observed trends.

Although the CosmoZoom simulations are offset with respect to the observed trends in the α_{av}–$M_\star$ diagram, they exhibit a similar trend as in the data, with mass density slope increasing (becoming shallower) with galaxy mass. The existence of such trend can be explained by a smaller amount of dissipation during the formation of high-, relative to low-, mass galaxies. During a merger, gas dissipates its kinetic energy, falling into the galaxy centre and forming new stars. Therefore, a higher level of dissipation leads to a more prominent contribution from newly formed stars to the total mass density in the centre, steepening the total density slope, as observed in low- relative to high-mass (both observed and simulated) ETGs. The existence of a strong correlation between density slope and radius (Section 5) also supports this interpretation, as dissipation would favour the formation of a smaller size system.

7 SUMMARY AND CONCLUSIONS

In this work, we have analysed the stellar and DM distribution in the central regions of ETGs, using a large sample of nearby galaxies from the SPIDER sample (La Barbera et al. 2010), as well as a complementary data set of ATLAS^{3D} ETGs (Cappellari et al. 2011). We have compared our findings to independent results from the literature, and predictions from numerical simulations. We have modelled each galaxy with two components, a Sérsic (de Vaucouleurs) profile for the SPIDER (ATLAS^{3D}) sample plus a variety of viable profiles for the DM distribution. Our reference model is based on an NFW (DM) plus a Sérsic (stars) component, assuming a concentration–virial mass relation from simulations (Macciò et al. 2008) and the virial to stellar mass relation of Moster et al. (2010). Assuming circular symmetry, no rotation, and neglecting radial gradients of the stellar mass-to-light ratio, Υ_*, in ETGs, we derive the only free parameter of the model, the Υ_*, from the central velocity dispersion, σ_{Ap} and σ_e, of each galaxy. None of these assumptions is found to affect significantly our results. From the two-component

models, we derive the total-mass density slope in the central regions of ETGs, and analyse its correlation with several galaxy parameters, i.e. σ_e, $M_\star$, R_e, and n. Our analysis (i) extends, with an independent approach, down to $M_\star \sim 10^{10}M_\odot$, the results of gravitational lensing studies of massive galaxies (Bolton et al. 2006, 2008; Auger et al. 2009, 2010); (ii) complements previous work (e.g. HB10; DT14; Chae et al. 2014; Oguri et al. 2014) by targeting two independent, large, samples of ETGs, and using a better tracer (the *K*-band light) of the stellar mass distribution in galaxies; and (iii) investigates the impact of a variety of modelling ingredients on the inferred Υ_* and central mass density slopes.

Our results can be summarized as follows.

(i) Consistent with our previous work (Tortora et al. 2013), we find that ETGs at high σ_e have larger Υ_* than that expected for a Chabrier IMF when fitting either colours or galaxy spectra with stellar population models, i.e. that the mismatch parameter, $\delta_{IMF} = \Upsilon_*/\Upsilon_*^{Chab}$, becomes significantly larger than one at high σ_e. This result can be interpreted as a systematic variation of the IMF normalization (i.e. the amount of stellar mass in the IMF) with σ_e. In this work, we find that δ_{IMF} also increases with stellar mass and R_e (but to less extent than the trend with σ_e), while it decreases with the Sérsic n. Using ATLAS^{3D} sample we find, on average, larger Υ_* and shallower correlations with all the parameters. These results are consistent with studies of gravity-sensitive features in ETGs, finding that the IMF becomes bottom-heavier than a 'standard', MW-like, distribution in high-, relative to low-σ_e ETGs (e.g. Ferreras et al. 2013; La Barbera et al. 2013; Spiniello et al. 2014). At low σ_e ($\sim$100 km s^{-1}), the value of δ_{IMF} ($\sim$1) implies a MW-like IMF normalization, consistent with results for late-type galaxies (Brewer et al. 2012; Sonnenfeld et al. 2012), and the combined lensing and stellar population analysis of Ferreras, Saha & Burles (2008) and Ferreras et al. (2010). The trends of δ_{IMF} hold for all DM profiles explored in this work, with lower δ_{IMF}'s for contracted halo and 'high-concentration' models (the latter being based on the c_{vir}–M_{vir} relation from LFS12).

(ii) For our reference model (see above), the total-mass density slope in the centre of ETGs increases (becoming less negative) with galaxy mass and galaxy size. For the ATLAS^{3D} sample, we find consistent results to those for SPIDER ETGs, although the trend with mass is steeper for the latter. In more detail, we find that low-mass (small) ETGs have slopes consistent with those for constant-M/L profiles, while massive (large R_e) systems have a nearly isothermal density slope ($=-2$), consistent with gravitational lensing results (e.g. Gavazzi et al. 2007; Auger et al. 2010). The trends of mass density slope are consistent with independent results from the literature (HB10; DT14). In terms of central velocity dispersion, the density slope decreases with central velocity dispersion (but to less extent than the amount of variation with R_e), while it exhibits a double-value behaviour with the Sérsic n, increasing at both low and high n, with a minimum for n between 3 and 5 (depending on the method to compute the slope).

(iii) The trends of mass density slope are the same for NFW and contracted-NFW models, and do not change when assuming a fixed virial mass (and concentration) for all galaxies (rather than a virial to stellar mass relation, such as that of Macciò et al. 2008). When adopting a Burkert profile, the slope tends to be more constant as a function of all galaxy parameters explored. However, for the most massive ETGs, the 'light' haloes described by Burkert models seem to be rejected by lensing results (Auger et al. 2009; see also Cardone & Tortora 2010).

(iv) Using a c_{vir}–M_{vir} relation from observations (LFS12) rather than simulations (Macciò et al. 2008) affects significantly some trends of density slope with galaxy parameters. In particular, while the slope keeps increasing with galaxy radius also for 'high-concentration' models (with c_{vir}–M_{vir} from LFS12), the trends with mass become flatter in this case. On the other hand, the trends with central velocity dispersion are the same for all models.

Our results corroborate a picture whereby the total-mass density profile in the central regions of ETGs is 'non-homologous', approaching a constant-M/L distribution at low mass – where stars dominate the total mass budget in the centre – and an isothermal profile in the most massive ETGs, whose central regions are more DM dominated. The fact that the mass density slope of groups and clusters of galaxies seems to be shallower than that of massive galaxies (e.g. Sand et al. 2008; HB10) further supports the 'non-homology' of the total mass distribution of galactic systems.

To understand the implications of our findings in the framework of galaxy assembly, we have also compared our results, i.e. the trends of total-mass density slope, with simulation predictions from R13. The comparison indicates that BH growth and feedback are essential ingredients during the formation of ETGs, as only simulations including them are able to reproduce the mass density slope, DM fraction, and stellar mass we have measured in the central regions of ETGs. Also, we find that both observations and simulations predict an increase of the total-mass density slope with galaxy mass. We argue that this trend is because gas dissipation has been more important during the formation of low-, relative to high-, mass galaxies. In such a picture, a steep profile is due to the formation of new stars inwards, as the gas, dissipating its kinetic energy, falls into the galaxy central regions, while gas-poor mergers tend to make the slopes isothermal.

This work shows that observations and simulations are now converging to provide a consistent characterization of the luminous and DM components in the central regions of ETGs. Nevertheless, important questions remain still open, like the discrepancy between halo concentration and mass from *N*-body simulations, and those obtained from lensing studies. In the future, it will be important to extend our results to the outermost regions of these galaxies, taking advantage of data covering a wide galactocentric baseline (e.g. kinematical tracers as planetary nebulae or globular clusters, Romanowsky et al. 2009; Napolitano et al. 2009, 2011; Pota et al. 2013) and accounting for radial gradients of the stellar IMF (Martín-Navarro et al. 2014; Pastorello et al. 2014). From the theoretical viewpoint, it will be also interesting to explore phenomenologically motivated models for the mass distribution in galaxies (e.g. Zhao 1997; Tortora, Cardone & Piedipalumbo 2007; Cardone et al. 2009), as well as alternative theories with modified gravity, like MOND (Milgrom 1983a, 1983b; Cardone et al. 2011a; Tortora et al. 2014) and modifications of the Einstein theory (e.g. *f*(*R*); Lubini et al. 2011; Napolitano et al. 2012).

ACKNOWLEDGEMENTS

We thank the referee for the kind report. CT has received funding from the European Union Seventh Framework Programme (FP7/2007-2013) under grant agreement no. 267251.

REFERENCES

Auger M. W., Treu T., Bolton A. S., Gavazzi R., Koopmans L. V. E., Marshall P. J., Bundy K., Moustakas L. A., 2009, ApJ, 705, 1099

Auger M. W., Treu T., Bolton A. S., Gavazzi R., Koopmans L. V. E., Marshall P. J., Moustakas L. A., Burles S., 2010, ApJ, 724, 511
Benson A. J., Cole S., Frenk C. S., Baugh C. M., Lacey C. G., 2000, MNRAS, 311, 793
Blumenthal G. R., Faber S. M., Flores R., Primack J. R., 1986, ApJ, 301, 27
Bolton A. S., Burles S., Koopmans L. V. E., Treu T., Moustakas L. A., 2006, ApJ, 638, 703
Bolton A. S., Burles S., Koopmans L. V. E., Treu T., Gavazzi R., Moustakas L. A., Wayth R., Schlegel D. J., 2008, ApJ, 682, 964
Brewer B. J. et al., 2012, MNRAS, 422, 3574
Bruzual G., Charlot S., 2003, MNRAS, 344, 1000
Buote D. A., Gastaldello F., Humphrey P. J., Zappacosta L., Bullock J. S., Brighenti F., Mathews W. G., 2007, ApJ, 664, 123
Burkert A., 1995, ApJ, 447, L25
Cappellari M. et al., 2006, MNRAS, 366, 1126
Cappellari M. et al., 2011, MNRAS, 413, 813
Cappellari M. et al., 2012, Nature, 484, 485
Cappellari M. et al., 2013a, MNRAS, 432, 1709
Cappellari M. et al., 2013b, MNRAS, 432, 1862
Cardone V. F., Tortora C., 2010, MNRAS, 409, 1570
Cardone V. F., Tortora C., Molinaro R., Salzano V., 2009, A&A, 504, 769
Cardone V. F., Angus G., Diaferio A., Tortora C., Molinaro R., 2011a, MNRAS, 412, 2617
Cardone V. F., Del Popolo A., Tortora C., Napolitano N. R., 2011b, MNRAS, 416, 1822
Chabrier G., 2001, ApJ, 554, 1274
Chae K.-H., Bernardi M., Kravtsov A. V., 2014, MNRAS, 437, 3670
Ciotti L., 1991, A&A, 249, 99
Conroy C., van Dokkum P. G., 2012, ApJ, 760, 71
de Blok W. J. G., McGaugh S. S., Bosma A., Rubin V. C., 2001, ApJ, 552, L23
de Vaucouleurs G., 1948, Ann. Astrophys., 11, 247
Del Popolo A., 2009, ApJ, 698, 2093
Dutton A. A., Treu T., 2014, MNRAS, 438, 3594 (DT14)
Dutton A. A. et al., 2011, MNRAS, 416, 322
Dutton A. A., Mendel J. T., Simard L., 2012, MNRAS, 422, L33
Dutton A. A., Macciò A. V., Mendel J. T., Simard L., 2013, MNRAS, 432, 2496
Ferreras I., Saha P., Burles S., 2008, MNRAS, 383, 857
Ferreras I., Saha P., Leier D., Courbin F., Falco E. E., 2010, MNRAS, 409, L30
Ferreras I., La Barbera F., de la Rosa I. G., Vazdekis A., de Carvalho R. R., Falcón-Barroso J., Ricciardelli E., 2013, MNRAS, 429, L15
Gavazzi R., Treu T., Rhodes J. D., Koopmans L. V. E., Bolton A. S., Burles S., Massey R. J., Moustakas L. A., 2007, ApJ, 667, 176
Gerhard O., Kronawitter A., Saglia R. P., Bender R., 2001, AJ, 121, 1936
Gnedin O. Y., Kravtsov A. V., Klypin A. A., Nagai D., 2004, ApJ, 616, 16
Goudfrooij P., Kruijssen J. M. D., 2013, ApJ, 762, 107
Goudfrooij P., Kruijssen J. M. D., 2014, ApJ, 780, 43
Humphrey P. J., Buote D. A., 2010, MNRAS, 403, 2143 (HB10)
Koopmans L. V. E. et al., 2009, ApJ, 703, L51
La Barbera F., de Carvalho R. R., Kohl-Moreira J. L., Gal R. R., Soares-Santos M., Capaccioli M., Santos R., Sant'anna N., 2008, PASP, 120, 681
La Barbera F., de Carvalho R. R., de La Rosa I. G., Lopes P. A. A., Kohl-Moreira J. L., Capelato H. V., 2010, MNRAS, 408, 1313
La Barbera F., Ferreras I., Vazdekis A., de la Rosa I. G., de Carvalho R. R., Trevisan M., Falcón-Barroso J., Ricciardelli E., 2013, MNRAS, 433, 3017
Leier D., Ferreras I., Saha P., 2012, MNRAS, 424, 104 (LFS12)
Lubini M., Tortora C., Näf J., Jetzer P., Capozziello S., 2011, Eur. Phys. J. C, 71, 1834
Macciò A. V., Dutton A. A., van den Bosch F. C., 2008, MNRAS, 391, 1940
Marinoni C., Hudson M. J., 2002, ApJ, 569, 101
Martín-Navarro I., La Barbera F., Vazdekis A., Falcón-Barroso J., Ferreras I., 2014, preprint (arXiv:1404.6533)
Martizzi D., Teyssier R., Moore B., 2014, MNRAS, 443, 1500
Memola E., Salucci P., Babić A., 2011, A&A, 534, A50 (MSB11)
Milgrom M., 1983a, ApJ, 270, 365
Milgrom M., 1983b, ApJ, 270, 371
Moore B., Governato F., Quinn T., Stadel J., Lake G., 1998, ApJ, 499, L5
Moster B. P., Somerville R. S., Maulbetsch C., van den Bosch F. C., Macciò A. V., Naab T., Oser L., 2010, ApJ, 710, 903
Napolitano N. R. et al., 2009, MNRAS, 393, 329
Napolitano N. R., Romanowsky A. J., Tortora C., 2010, MNRAS, 405, 2351
Napolitano N. R. et al., 2011, MNRAS, 411, 2035
Napolitano N. R., Capozziello S., Romanowsky A. J., Capaccioli M., Tortora C., 2012, ApJ, 748, 87
Navarro J. F., Frenk C. S., White S. D. M., 1996, ApJ, 462, 563 (NFW)
Navarro J. F., Frenk C. S., White S. D. M., 1997, ApJ, 490, 493
Oguri M., Rusu C. E., Falco E. E., 2014, MNRAS, 439, 2494
Pastorello N., Forbes D. A., Foster C., Brodie J. P., Usher C., Romanowsky A. J., Strader J., Arnold J. A., 2014, MNRAS, 442, 1003
Pota V. et al., 2013, MNRAS, 428, 389
Remus R.-S., Burkert A., Dolag K., Johansson P. H., Naab T., Oser L., Thomas J., 2013, ApJ, 766, 71 (R13)
Romanowsky A. J., Strader J., Spitler L. R., Johnson R., Brodie J. P., Forbes D. A., Ponman T., 2009, AJ, 137, 4956
Salpeter E. E., 1955, ApJ, 121, 161
Salucci P., Burkert A., 2000, ApJ, 537, L9
Sand D. J., Treu T., Ellis R. S., Smith G. P., Kneib J.-P., 2008, ApJ, 674, 711
Shu Y. et al., 2014, preprint (arXiv:1407.2240)
Sonnenfeld A., Treu T., Gavazzi R., Marshall P. J., Auger M. W., Suyu S. H., Koopmans L. V. E., Bolton A. S., 2012, ApJ, 752, 163
Spiniello C., Trager S. C., Koopmans L. V. E., Chen Y. P., 2012, ApJ, 753, L32
Spiniello C., Trager S., Koopmans L. V. E., Conroy C., 2014, MNRAS, 438, 1483
Swindle R., Gal R. R., La Barbera F., de Carvalho R. R., 2011, AJ, 142, 118
Thomas J., Saglia R. P., Bender R., Thomas D., Gebhardt K., Magorrian J., Corsini E. M., Wegner G., 2009, ApJ, 691, 770
Thomas J. et al., 2011, MNRAS, 415, 545
Tortora C., Cardone V. F., Piedipalumbo E., 2007, A&A, 463, 105
Tortora C., Antonuccio-Delogu V., Kaviraj S., Silk J., Romeo A. D., Becciani U., 2009a, MNRAS, 396, 61
Tortora C., Napolitano N. R., Romanowsky A. J., Capaccioli M., Covone G., 2009b, MNRAS, 396, 1132
Tortora C., Napolitano N. R., Romanowsky A. J., Jetzer P., Cardone V. F., Capaccioli M., 2011, MNRAS, 418, 1557
Tortora C., La Barbera F., Napolitano N. R., de Carvalho R. R., Romanowsky A. J., 2012, MNRAS, 425, 577
Tortora C., Romanowsky A. J., Napolitano N. R., 2013, ApJ, 765, 8
Tortora C., Romanowsky A. J., Cardone V. F., Napolitano N. R., Jetzer P., 2014, MNRAS, 438, L46
Treu T., Koopmans L. V. E., 2004, ApJ, 611, 739
Treu T., Auger M. W., Koopmans L. V. E., Gavazzi R., Marshall P. J., Bolton A. S., 2010, ApJ, 709, 1195
van den Bosch F. C. et al., 2007, MNRAS, 376, 841
Vazdekis A., Ricciardelli E., Cenarro A. J., Rivero-González J. G., Díaz-García L. A., Falcón-Barroso J., 2012, MNRAS, 3156
Wegner G. A., Corsini E. M., Thomas J., Saglia R. P., Bender R., Pu S. B., 2012, AJ, 144, 78
Weidner C., Ferreras I., Vazdekis A., La Barbera F., 2013, MNRAS, 435, 2274
Wolf J., Martinez G. D., Bullock J. S., Kaplinghat M., Geha M., Muñoz R. R., Simon J. D., Avedo F. F., 2010, MNRAS, 406, 1220
Zhao H., 1997, MNRAS, 287, 525

This paper has been typeset from a TEX/LATEX file prepared by the author.